Journal of the Mechanics and Physics of Solids, 50 : 2002, 1789-1815

A COMPUTATIONAL MODEL FOR THE INDENTATION AND PHASE TRANSFORMATION OF A MARTENSITIC THIN FILM

PAVEL BĚLÍK AND MITCHELL LUSKIN

Abstract. We propose a computational model for a stress-induced martensitic phase transformation of a single-crystal thin film by indentation and its reverse transformation to austenite by heating. Our model utilizes a surface energy that allows sharp interfaces with finite energy and a penalty that forces the film to lie above the indenter and undergo a stress-induced austenite-to-martensite phase transformation. We introduce a method to nucleate the martensite-to-austenite phase transformation since in our model the film would otherwise remain in the martensitic phase in a local minimum of the energy.

1. Introduction

Due to the growing interest in microdevices utilizing shape-memory materials [21], much research has focused on understanding the behavior of these materials, particularly martensitic alloys. A geometrically nonlinear theory of martensite has been developed [2, 3] and corresponding thin film theories have been derived [6, 9]. Thin films of single-crystal martensitic alloys have recently been grown [15], and the miniaturization of devices using these films is being pursued.

It is the goal of this paper to demonstrate the feasibility of simulating the deformation of martensitic single-crystal thin films during thermally activated and stress-induced phase changes by numerically modeling an experiment of Cui and James [14]. This experiment confirmed the prediction of the thin film theory that certain alloys of specific composition and orientation have the martensitic tent described in [6] as a local minimum of the energy. A thin film of CuAlNi with a specific composition and orientation was subjected to a suitable heat treatment, and an indenter in the shape of the tent predicted by the thin film theory [6] was used to deform the film appropriately. Upon removal of the indenter, the film remained in the tent-like shape. A water bath was used to heat the film so that it transformed back to austenite, and the experiment was repeated several times.

We extend the mathematical model and numerical methods described in [7] for a pressurized film to numerically simulate this experiment. Our computational model utilizes a penalty to force the film to lie above the indenter and undergo a stress-induced austenite-to-martensite phase transformation and a total variation surface energy that allows sharp phase boundaries of finite energy [9]. Our total variation thin film model also allows us to develop a method to nucleate the martensite-to-austenite phase transformation. The nucleation step in our algorithm is needed since the film would otherwise remain in the martensitic phase in a local minimum of the energy. Our numerical results show good qualitative agreement with the experiment.

Date: August 13, 2001.

Key words and phrases. Thin film, martensite, austenite, phase transformation, nucleation.

This work was supported in part by NSF DMS 95-05077, by NSF DMS-0074043, by AFOSR F49620-98-1-0433, by ARO DAAG55-98-1-0335, by the Institute for Mathematics and Its Applications, and by the Minnesota Supercomputer Institute.

In Section 2, we briefly describe the experiment performed by Cui and James with a thin film of Cu-Al(wt.%)13.95-Ni(wt.%)3.93. In Section 3, we describe the mathematical models we have used to compute the deformation of martensitic thin films [6, 9].

Although the long-term goal of our research is the development of the capability to predict the quantitative behavior of martensitic single-crystal thin films, we are concerned at this initial stage with the exploration and validation of mathematical models. Nonetheless, we have used measured elastic moduli and transformation strains when available, although other physical constants have been chosen to explore the properties of the model. In Section 4, we describe the properties of the elastic energy density. Since we did not have the elastic moduli for Cu-Al(wt.%)13.95-Ni(wt.%)3.93, the elastic density that we use was constructed to match the transformation strains and the measured austenitic and martensitic elastic moduli for some related copper-based shape memory alloys with similar crystallography [4, 18, 19].

Section 5 summarizes the theoretical conditions on the alloy for the tent deformation to a local minimum of the energy. We apply these conditions to a CuZnAl alloy to determine the necessary orientation of a thin film of this material to satisfy the conditions for the tent to be a local minimum of the energy, and we describe the obstacle problem for the indenter experiment and devise a penalty method to model it. The finite element approximation is given in Section 6, and the results of the numerical simulation of the indenting stage of the experiment are presented in Section 7.

The description of the model for the heating process of the experiment and the numerical simulations for this process are presented in Sections 8 and 9, respectively. We introduce a method to nucleate the martensite-to-austenite phase change since otherwise the film would remain in the martensitic phase in a local minimum of the energy. In Section 10, we give an analysis to explore the effect of energy barriers on the numerical solution.

Finally, in Section 11, we present results for the solution to the indenter problem when the crystal does not exactly satisfy the tent compatibility conditions. This is actually the case for the Cu-Zn(at.%)15-Al(at.%)17 alloy [10].

2. Description of the Indenter Experiment

In this section, we describe the experiment performed by Cui and James [14]. The specimen used in this experiment was Cu-Al(wt.%)13.95-Ni(wt.%)3.93 heat-treated so that it undergoes a cubic-to-monoclinic transformation. It is shown in [14] that it very closely satisfies the necessary compatibility conditions formulated in [6] for a suitably oriented thin film to have a tent deformation as a local minimum of the energy. The thin film used in the experiment was obtained by polishing a slice of the alloy at high temperature to obtain a film with thickness 0.04 ± 0.01 mm.

The indenter was made of PVC and was machined with an orientation required by the thin film theory for the existence of a stress-free tent with martensitic sides (Figure 1(a)). The fixture used to hold the film is depicted in Figure 1(b). The film in its austenitic phase was suitably oriented and tightly attached, but left loose in a middle square area with size equal to that of the indenter (approximately 1 cm by 1 cm). A water bath was used to control the temperature of the film. The fluid was brought into the fixture through two plastic tubes on the side of the fixture and circulated around the edges of the film.

To obtain the tent, the temperature was lowered to 10°C and held constant for about 15 minutes. Then, the indenter was pushed into the film, and a tent deformation was observed. After the indenter was removed, the film slightly dropped, but stayed in the shape of a tent (Figure 2). It was verified by microdiffraction that most of the film on each side of the tent was in a single variant of martensite. This X-ray method was not conclusive close to the lower edges of the tent as different variants of martensite were detected.

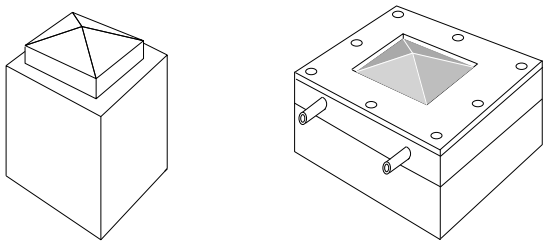

(a) (b)

FIGURE 1. The indenter and the fixture used in the experiment. Courtesy of J. Cui and R. James.

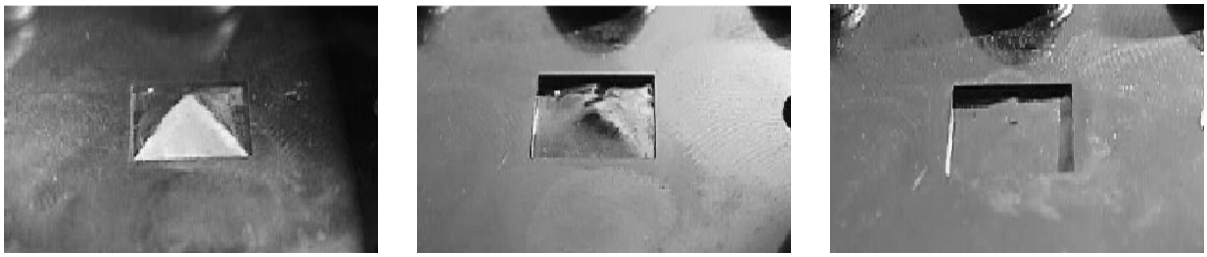

(a) (b) (c)

FIGURE 2. (a) The tent deformation of Cu-Al(wt.%)13.95-Ni(wt.%)3.93 at 10°C on a film of thickness 40 μm with surface normal [100] and edge $[0, 4.331, 1]$. The size of the tent is $0.4 \times 0.4 \times 0.188$ inches. (b) and (c) The tent at 70°C and 90°C during the heating phase. Courtesy of J. Cui and R. James.

After obtaining the tent, the temperature of the water bath surrounding the film was slowly increased to 95°C, which caused the tent to start to gradually shrink and collapse (Figure 2). Until the tent had shrunk to about two-thirds of its original size, the shape of the tent was almost identical to the original shape. Then the shape started to change—all the edges became rounded. This process continued until most of the film transformed back to its original flat shape. The very tip of the tent, where perhaps some plastic deformation occurred, took about thirty minutes to flatten out. The indenting and heating procedures were repeated four times and the tent deformation and the flat shape were completely recovered each time; however, after the fifth cycle a little bulge remained visible on the surface of the film even after two hours of heating. This was viewed as a result of permanent plastic deformation.

3. Thin Film Models

We assume that the energy density $\phi(F, \theta)$ is a continuous function $\phi : \mathbb{R}^{3\times 3} \times (\theta_0, \theta_1) \to \mathbb{R}$ representing the energy per unit reference volume of the material as a function of the deformation gradient $F \in \mathbb{R}^{3\times 3}$ and the temperature $\theta \in (\theta_0, \theta_1)$ where $\theta_0 < \theta_c < \theta_1$ for the transformation temperature θ_c at which the austenitic and martensitic phases have the same free energy density. We can assume that the energy density ϕ satisfies the growth condition

$$c_1|F|^p - c_2 \leq \phi(F, \theta) \leq c_3(|F|^p + 1) \quad \text{for all } F \in \mathbb{R}^{3\times 3} \text{ and } \theta \in (\theta_0, \theta_1), \tag{3.1}$$

where c_1, c_2, and c_3 are fixed positive constants. This growth condition controls the behavior of $\phi(F,\theta)$ as $|F|$ tends to infinity; however, in all of our simulations the deformation gradient remains near the bottoms of the energy wells and hence we do not worry about the growth of ϕ at infinity.

In our computations, we have used the total-variation thin film energy rigorously derived by the authors in [9] following earlier work on a strain gradient model by Bhattacharya and James [6]. Discussions of the modeling and scaling of surface energy can be found in [2, 20]. Our model gives a finite surface energy to sharp austenite-martensite and martensite-martensite interfaces and allows the use of continuous, piecewise linear finite elements for the deformation while retaining surface energy in the model [9]. We have given numerical results to compare the difference between solutions computed with small surface energy (Figure 5) and solutions computed with no surface energy (Figure 6).

In our total-variation surface energy model, the bulk energy for a film of thickness $h > 0$ with reference configuration $\Omega_h \equiv \Omega \times (-h/2,\ h/2)$, where $\Omega \subset \mathbb{R}^2$ is a domain with a Lipschitz continuous boundary $\partial\Omega$, is given by the sum of the surface energy and the elastic energy

$$\kappa \int_{\Omega_h} |D(\nabla u)| + \int_{\Omega_h} \phi(\nabla u, \theta)\, dx \tag{3.2}$$

where $\int_{\Omega_h} |D(\nabla u)|$ is the total variation of the deformation gradient [9] and κ is a small positive constant. The total variation of a deformation gradient ∇u that has discontinuities across the piecewise smooth surfaces $\sigma_j,\ j = 1, \ldots, J$, separating the open sets ω_ℓ in the disjoint union $\Omega_h = \sum_{\ell=1}^{L} \omega_\ell$ is given by

$$\int_{\Omega_h} |D(\nabla u)| = \sum_{j=1}^{J} \int_{\sigma_j} |[\![\, \nabla u \,]\!]_{\sigma_j}|\, dS + \sum_{\ell=1}^{L} \int_{\omega_\ell} \sqrt{\sum_{m,n=1}^{3} \left(\frac{\partial^2 u}{\partial x_m \partial x_n} \right)^2}\, dx$$

where $|[\![\, \nabla u \,]\!]_{\sigma_j}|$ denotes the euclidean norm of the jump of the deformation gradient across the interface σ_j. The film is assumed to be bonded at $\partial\Omega \times (-h/2,\ h/2)$, so the admissible deformations are constrained by the boundary condition

$$u(x_1, x_2, x_3) = y_0(x_1, x_2) + b_0(x_1, x_2)x_3 \quad \text{for } (x_1, x_2) \in \partial\Omega,\ x_3 \in (-h/2,\ h/2),$$

for fixed functions $y_0,\ b_0$.

It has been shown in [9] that energy-minimizing deformations u of the bulk energy (3.2) are asymptotically of the form

$$u(x_1, x_2, x_3) = y(x_1, x_2) + b(x_1, x_2)x_3 + \mathrm{o}(x_3^2) \quad \text{for } (x_1, x_2) \in \Omega,\ x_3 \in (-h/2,\ h/2), \tag{3.3}$$

where (y, b) minimizes the thin film energy

$$\mathcal{E}(y, b, \theta) = \kappa \left(\int_\Omega |D(\nabla y | b | b)| + \sqrt{2} \int_{\partial\Omega} |b - b_0| \right) + \int_\Omega \phi(\nabla y | b, \theta)\, dx \tag{3.4}$$

over all deformations of finite energy such that $\tilde{y} = y_0$ on $\partial\Omega$. The map b describes the deformation of the cross-section relative to the film [6]. We denote by $(\nabla y | b) \in \mathbb{R}^{3\times 3}$ the matrix whose first two columns are given by the columns of ∇y and the last column by b and occasionally refer to it as the "deformation gradient." In the above equation, $\int_\Omega |D(\nabla y | b | b)|$ is the total variation of the vector valued function $(\nabla y | b | b) : \Omega \to \mathbb{R}^{3\times 4}$. An explicit computable formula for the total variation $\int_\Omega |D(\nabla y | b | b)|$ is given in Section 6 for finite element approximations.

The first integral in the expression for the energy (3.4) models the interfacial (or surface) energy. Since κ is typically small, the interfacial energy term is sometimes neglected by setting $\kappa = 0$ and

assuming that the free energy is given by the expression

$$\mathcal{E}(y,b,\theta) = \int_\Omega \phi(\nabla y|b,\theta)\,dx. \tag{3.5}$$

This greatly enlarges the space of admissible deformations since we no longer have to require that $\int_\Omega |D(\nabla y|b|b)| < \infty$. To ensure continuity of y up to the boundary, $\partial\Omega$, we may assume that $p > 2$ in (3.1) [1].

However, energy-minimizing deformations of the energy (3.5) do not exist for general boundary conditions since the minimum energy may only be approached by deformations whose gradients oscillate between energy wells across layers whose width converges to zero [2, 24]. The addition of the surface energy ($\kappa > 0$) gives a positive contribution to the energy for each oscillation of the deformation gradient across a layer, thus limiting the number of layers for energy-minimizing deformations and guaranteeing the existence of classical solutions [9, 20, 24]. Since the width of possible layers is bounded below by the mesh size for finite element approximations, the minimum of (3.4) restricted to finite element deformations exists even for $\kappa = 0$ [24].

In previous numerical simulations [7,11–13,22], it has been observed that even without imposing the condition that the deformed body not penetrate itself [17], this was indeed the case. Hence, we do not impose this condition on the space of admissible deformations. We note that these requirements have been satisfied by all of the numerical solutions that we have obtained in our simulations.

4. Elastic Energy Densities

We will construct a frame-indifferent energy density [17] with reference configuration given by the austenitic phase at the transformation temperature. We assume for simplicity that the unstressed austenitic state does not change for $\theta \in (\theta_0, \theta_1)$, so that it follows from the frame indifference of the energy density that $\phi(F,\theta)$ is minimized at $F \in \mathrm{SO}(3)$ for $\theta \geq \theta_c$ where $\mathrm{SO}(3)$ denotes the group of proper rotations. We also assume that the transformation strain U_1 for the unstressed martensitic phase does not vary for $\theta \in (\theta_0, \theta_1)$, so that the energy density is minimized for $\theta \leq \theta_c$ at

$$\mathcal{U} = \mathrm{SO}(3)U_1 \cup \cdots \cup \mathrm{SO}(3)U_N, \tag{4.1}$$

where for the symmetry group $\mathcal{G}$ of the austenitic phase we have

$$\{U_1, \ldots, U_N\} = \{R^T U_1 R : \ R \in \mathcal{G}\}. \tag{4.2}$$

As discussed in [6], certain thin films of single-crystal martensitic alloys with specific material constants support the formation of a four-sided tent each of whose sides is predicted to consist of a single variant of martensite, with opposite sides consisting of the same, but rotated, variant. The experimental indentation results of Cui and James [14] using X-ray diffraction confirmed that each side of the tent had transformed to the predicted variant. One of the goals of our simulations is to numerically reproduce the indenter experiment discussed in Section 2. For this reason, it is desirable to use an energy-density model constructed so that it fits as many elastic moduli and transformation strains for this alloy as possible. Since the elastic moduli and transformation strains for the CuAlNi alloy were not available to us, we utilized published elastic moduli and transformation strains for some CuZnAl alloys [4, 16, 28].

The CuZnAl alloy we consider undergoes a cubic-to-monoclinic transformation and thus has twelve ($N = 12$) variants. However, the theoretical [6] and experimental [6] results described above have led us for computational efficiency to utilize an energy density that is minimized only at the

wells with the maximal in-plane extensions generated by the four variants U_i, $i = 1, \dots, 4$, given by

$$U_1 = \begin{pmatrix} \alpha & \delta & 0 \\ \delta & \beta & 0 \\ 0 & 0 & \gamma \end{pmatrix}, \quad U_2 = \begin{pmatrix} \beta & \delta & 0 \\ \delta & \alpha & 0 \\ 0 & 0 & \gamma \end{pmatrix}, \quad U_3 = \begin{pmatrix} \alpha & -\delta & 0 \\ -\delta & \beta & 0 \\ 0 & 0 & \gamma \end{pmatrix}, \quad U_4 = \begin{pmatrix} \beta & -\delta & 0 \\ -\delta & \alpha & 0 \\ 0 & 0 & \gamma \end{pmatrix}, \quad (4.3)$$

with $\alpha, \beta, \gamma, \delta > 0$, $\alpha > \beta$, and $\alpha\beta - \delta^2 > 0$ [4, 8]. The parameters for Cu-Zn(at.%)15-Al(at.%)17 are [4, 10]

$$\alpha = 1.087, \quad \beta = 1.01, \quad \gamma = 0.9093, \quad \delta = 0.025.$$

The reduction to the four-well case (4.3) corresponds to a particular case of the tetragonal-to-monoclinic phase transformation [8] and therefore the energy densities W_M and $\bar{W}_M$ corresponding to the martensitic phase and defined below will have tetragonal symmetry. However, the energy density W_A corresponding to the austenitic phase will retain the cubic symmetry.

To construct our energy density, we construct energy densities $W_M(F)$ for the martensitic phase and $W_A(F)$ for the austenitic phase such that

$$\begin{aligned} W_M(F) = 0 \quad &\text{if and only if} \quad F \in \mathcal{U} = \mathrm{SO}(3)U_1 \cup \cdots \cup \mathrm{SO}(3)U_N, \\ W_A(F) = 0 \quad &\text{if and only if} \quad F \in \mathrm{SO}(3), \end{aligned}$$

and such that $W_M(F)$ and $W_A(F)$ approximately match the elastic moduli at their respective energy wells. We note that it is not possible to match all of the moduli with a reasonably simple energy density and that elastic moduli for specific alloy compositions are not always available in the published literature.

We will define the energy density $\phi(F, \theta)$, similarly as in [7], by

$$\phi(F,\theta) = \begin{cases} \min\left\{W_A(F),\ W_M(F) + \frac{(\theta-\theta_c)W_A(U_1)}{W_A(U_1)+(\theta-\theta_c)}\right\} & \text{for } \theta \geq \theta_c, \\ \min\left\{W_A(F) + \frac{(\theta_c-\theta)W_M(I)}{W_M(I)+(\theta_c-\theta)},\ W_M(F)\right\} & \text{for } \theta < \theta_c. \end{cases} \quad (4.4)$$

For the energy density $\phi(F, \theta)$, the minimum value is attained on SO(3) for $\theta \geq \theta_c$ and on $\mathcal{U}$ for $\theta \leq \theta_c$, and each of the energy wells SO(3) and $\mathcal{U}$ are local minimizers for all $\theta \in \mathbb{R}$. We note that this energy density has been normalized so that its minimum value is zero for all temperatures. A function of θ could be added to the energy density without changing the computations that we present in this paper.

To construct our energy density, we modify the quasi-convex energy density developed by Bhattacharya and Dolzmann [4, 5]. Their energy density is given by

$$\bar{W}_M(F) = a\left(\det F - (\alpha\beta - \delta^2)\gamma\right)^2 + b\left[|\operatorname{cof} F e_3|^2 - (\alpha\beta - \delta^2)^2\right]_+^2 + \sum_{i=1}^{13} c_i\left[|Fv_i|^2 - B_i\right]_+^2$$

for $v_i \in \mathbb{R}^3$, $B_i \in \mathbb{R}$ and constants $a, b, c_1, \dots, c_5 > 0$, $c_i \geq 0$ that satisfy

$$c_2 = c_3, \quad c_4 = c_5, \quad c_6 = \cdots = c_9, \quad c_{10} = \cdots = c_{13}.$$

We used above the notation that $[s]_+ = \max\{0, s\}$. The values of the constants a, b, and c_i given in Table 1 were determined in [4] to approximate the elastic moduli (in GPa) for Cu-Zn(at.%)12.8-Al(at.%)17.6 [28].

We have used $\bar{W}_M$ to construct a nonnegative function W_M that vanishes only on the union $\mathcal{U}$ of the martensitic wells (4.1), but preserves the martensitic elastic moduli of $\bar{W}_M$. Since the elastic moduli are determined by the second derivatives of W_M, it is only a matter of verifying that these

i	v_i	B_i	c_i
1	$(0,0,1)$	γ^2	1.97
2	$(1,1,0)$	$\alpha^2+\beta^2+2\delta(\alpha+\beta+\delta)$	0.12
3	$(1,-1,0)$	$\alpha^2+\beta^2+2\delta(\alpha+\beta+\delta)$	0.12
4	$(1,0,0)$	$\alpha^2+\delta^2$	9.76
5	$(0,1,0)$	$\alpha^2+\delta^2$	9.76
6	$(1,1,1)$	$\alpha^2+\beta^2+\gamma^2+2\delta(\alpha+\beta+\delta)$	3.0
7	$(-1,1,1)$	$\alpha^2+\beta^2+\gamma^2+2\delta(\alpha+\beta+\delta)$	3.0
8	$(1,-1,1)$	$\alpha^2+\beta^2+\gamma^2+2\delta(\alpha+\beta+\delta)$	3.0
9	$(1,1,-1)$	$\alpha^2+\beta^2+\gamma^2+2\delta(\alpha+\beta+\delta)$	3.0
10	$(1,0,1)$	$\alpha^2+\delta^2+\gamma^2$	0.38
11	$(1,0,-1)$	$\alpha^2+\delta^2+\gamma^2$	0.38
12	$(0,1,1)$	$\alpha^2+\delta^2+\gamma^2$	0.38
13	$(0,-1,1)$	$\alpha^2+\delta^2+\gamma^2$	0.38
$a=29.61$		$b=6.8$	

TABLE 1. The vectors and constants in the definition of $\bar{W}_M$ and W_M.

second derivatives of W_M, when evaluated at U_1, do not change from those of $\bar{W}_M$. The elastic moduli at the remaining U_i will then be matched by the tetragonal symmetry of the energy density.

We illustrate the idea for constructing the energy W_M from $\bar{W}_M$ by the following example. Assume that $\bar{w}:\mathbb{R}\to[0,+\infty)$ is given by $\bar{w}(x)=c[x-1]_+^2+c[-1-x]_+^2$ with $c>0$ so that it vanishes on the interval $[-1,1]$ and $\lim_{x\searrow 1}\bar{w}''(x)=\lim_{x\nearrow -1}\bar{w}''(x)=2c$. Then the function $w(x)\equiv\frac{c}{4}(x-1)^2(x+1)^2$ is nonnegative, vanishes at ±1, and $w''(\pm1)=2c$.

In our computations, we use the energy

$$
\begin{aligned}
W_M(F) &= a\left(\det F-(\alpha\beta-\delta^2)\gamma\right)^2+b\left(|\operatorname{cof}Fe_3|^2-(\alpha\beta-\delta^2)^2\right)^2+c_1\left(|Fv_1|^2-B_1\right)^2\\
&+\frac{c_2}{16\delta^2(\alpha+\beta)^2}\left(|Fv_2|^2-B_2\right)^2\left(|Fv_3|^2-B_3\right)^2+\frac{c_4}{\left(\alpha^2-\beta^2\right)^2}\left(|Fv_4|^2-B_4\right)^2\left(|Fv_5|^2-B_5\right)^2\\
&+\frac{c_6}{32\delta^2(\alpha+\beta)^2}\left[\left(|Fv_6|^2-B_6\right)^2+\left(|Fv_9|^2-B_9\right)^2\right]\cdot\left[\left(|Fv_7|^2-B_7\right)^2+\left(|Fv_8|^2-B_8\right)^2\right]\\
&+\frac{c_{10}}{2\left(\alpha^2-\beta^2\right)^2}\left[\left(|Fv_{10}|^2-B_{10}\right)^2+\left(|Fv_{11}|^2-B_{11}\right)^2\right]\cdot\left[\left(|Fv_{12}|^2-B_{12}\right)^2+\left(|Fv_{13}|^2-B_{13}\right)^2\right].
\end{aligned}
$$

The constants a, b, c_i, and B_i and the vectors v_i agree with those in the definition of $\bar{W}_M$ and are given in Table 1. We note that the energy density $W_M(F)$ also vanishes on a spurious set $\tilde{\mathcal{U}}=\mathrm{SO}(3)\tilde{U}_1\cup\cdots\cup\mathrm{SO}(3)\tilde{U}_N$ in addition to $\mathcal{U}=\mathrm{SO}(3)U_1\cup\cdots\cup\mathrm{SO}(3)U_N$. Since $\operatorname{tr}F^TF\approx 8.007$ for $F\in\tilde{U}$, we could add the term $[\operatorname{tr}F^TF-4]_+^2$ to the energy density to ensure that it does not have zero energy density on the spurious set $\tilde{\mathcal{U}}=\mathrm{SO}(3)\tilde{U}_1\cup\cdots\cup\mathrm{SO}(3)\tilde{U}_N$, but we did not need to do so since we never obtained such deformation gradients in our computations.

Next, we construct an energy density, W_A, corresponding to the austenitic phase. To this end, we recall that the parent austenitic phase of CuZnAl has cubic symmetry and so there are only three independent elastic moduli [23]. These have been measured for Cu-Zn(wt.%)21.4-Al(wt.%)5.9 [16]. Using the standard notation [23], we have from [16] that

$$\mathbb{C}_{11}=130\pm1\text{ GPa},\qquad \mathbb{C}_{44}=86\pm1\text{ GPa},$$

and

$$C_L = \tfrac{1}{2}\left(\mathbb{C}_{11} + \mathbb{C}_{12} + 2\mathbb{C}_{44}\right) = 203 \pm 2 \text{ GPa}, \qquad C' = \tfrac{1}{2}\left(\mathbb{C}_{11} - \mathbb{C}_{12}\right) = 5.8 \pm 0.2 \text{ GPa},$$
$$A = \frac{2\mathbb{C}_{44}}{\mathbb{C}_{11} - \mathbb{C}_{12}} = 15 \pm 1.$$

It is easy to see that it is not possible to choose $\mathbb{C}_{11}$, $\mathbb{C}_{12}$, and $\mathbb{C}_{44}$ so that all of the above quantities fall within the given ranges. Hence, we take

$$\mathbb{C}_{11} = 130 \text{ GPa}, \qquad \mathbb{C}_{12} = 118.4 \text{ GPa}, \qquad \mathbb{C}_{44} = 86 \text{ GPa},$$

so that

$$C_L = 210.2 \text{ GPa}, \qquad C' = 5.8 \text{ GPa}, \qquad A \approx 14.8.$$

A simple example of a function W_A that is frame-indifferent, has cubic symmetry, vanishes only on the set SO(3), and has the elastic moduli $\mathbb{C}_{11}$, $\mathbb{C}_{12}$, and $\mathbb{C}_{44}$ is

$$W_A(F) = d\left(\det F - 1\right)^2 + e\left(C_{12}^2 + C_{13}^2 + C_{23}^2\right) + f\left[\left(C_{11} - 1\right)^2 + \left(C_{22} - 1\right)^2 + \left(C_{33} - 1\right)^2\right],$$

where $C = F^T F$ is the Cauchy-Green strain corresponding to the deformation gradient F and

$$d = \tfrac{1}{2}\,\mathbb{C}_{12}, \qquad e = \tfrac{1}{2}\,\mathbb{C}_{44}, \qquad f = \tfrac{1}{8}\left(\mathbb{C}_{11} - \mathbb{C}_{12}\right).$$

We will also experiment numerically with the energy density $\bar{\phi}$ defined by

$$\bar{\phi}(F,\theta) = \begin{cases} \min\left\{W_A(F),\ \bar{W}_M(F) + \frac{(\theta-\theta_c)W_A(U_1)}{W_A(U_1)+(\theta-\theta_c)}\right\} & \text{for } \theta \geq \theta_c, \\ \min\left\{W_A(F) + \frac{(\theta_c-\theta)\bar{W}_M(I)}{\bar{W}_M(I)+(\theta_c-\theta)},\ \bar{W}_M(F)\right\} & \text{for } \theta < \theta_c. \end{cases} \tag{4.5}$$

The minimum of $\bar{\phi}(F,\theta)$ is attained on SO(3) for $\theta \geq \theta_c$ and on the quasi-convex hull $\mathcal{U}^{qc}$ [4] for $\theta \leq \theta_c$. We also have that each of the energy wells SO(3) and $\mathcal{U}^{qc}$ are local minimizers for all $\theta \in \mathbb{R}$. We note that $\bar{\phi}$ is not quasi-convex, although the martensitic energy density $\bar{W}_M(F)$ is quasi-convex [4].

5. Tent Deformation

We now show that for a slight change of the parameter δ there exists a stress-free tent deformation of a square surface orthogonal to e_3 with faces in the martensitic phase [6]. We note that $R(\pi/2, e_3)^T U_1 R(\pi/2, e_3) = U_4$ where $R(\pi/2, e_3) \in \text{SO}(3)$ is the rotation of $\pi/2$ radians about e_3. It thus follows from the theory of Bhattacharya and James [6] that there exists such a square surface orthogonal to e_3 with a side parallel to $e \in \mathbb{R}^3$, $|e| = 1$, $e \cdot e_3 = 0$, along which that tent has deformation gradient RU_1 for $R \in \text{SO}(3)$ if and only if there exists $Q \in \text{SO}(3)$ such that

$$\begin{aligned} &QU_1 e = e, \\ &QU_1 n \cdot QU_1 e = U_1 n \cdot U_1 e = 0 \qquad \text{for } n = e_3 \times e, \\ &|QU_1 n| = |U_1 n| > 1. \end{aligned} \tag{5.1}$$

Since the subspace $\{v \in \mathbb{R}^3 :\ v \cdot e_3 = 0\}$ is invariant for U_1, necessary and sufficient conditions for the existence of a tent can be given that are much simpler than those given for the general case in [6]. It is easy to see that (5.1) holds if and only if $Q = R(\chi, e)$ for any rotation of χ radians about e and

$$U_1 = e \otimes e + \lambda n \otimes n + \gamma e_3 \otimes e_3 \tag{5.2}$$

for $\lambda > 1$. If (5.1) holds, then a stress-free tent deformation can be formed with sides having deformation gradient $R(\chi, e)U_1$, $R(\chi, n)U_4$, $R(-\chi, e)U_1$, and $R(-\chi, n)U_4$ for $\chi = \pm \arccos \lambda^{-1}$.

Now the eigenvalues of U_1 are

$$\frac{(\alpha+\beta) \pm \sqrt{(\alpha-\beta)^2+4\delta^2}}{2},\ \gamma.$$

Since $\alpha > 1$ and $\beta > 1$, we see that the larger eigenvalue satisfies

$$\frac{(\alpha+\beta) + \sqrt{(\alpha-\beta)^2+4\delta^2}}{2} > 1,$$

but the smaller eigenvalue satisfies

$$\frac{(\alpha+\beta) - \sqrt{(\alpha-\beta)^2+4\delta^2}}{2} \neq 1$$

for $\alpha = 1.087$, $\beta = 1.01$, $\delta = 0.025$. However,

$$\frac{(\alpha+\beta) - \sqrt{(\alpha-\beta)^2+4\tilde{\delta}^2}}{2} = 1$$

for

$$\tilde{\delta} = \sqrt{(\alpha-1)(\beta-1)} \approx 0.0295.$$

We shall use the value $\delta = \tilde{\delta} = 0.0295$ in our subsequent computations to guarantee the existence of a stress-free tent. We shall also present computational results for the measured value $\delta = 0.025$ in Section 11 to investigate solutions of our thin film model when the tent conditions are not exactly satisfied.

It can be checked that for $\delta = \tilde{\delta}$ we have that

$$\begin{aligned}
e &= (\alpha+\beta-2)^{-1/2}\left(\sqrt{\beta-1},\ -\sqrt{\alpha-1},\ 0\right),\\
n &= (\alpha+\beta-2)^{-1/2}\left(\sqrt{\alpha-1}, \sqrt{\beta-1},\ 0\right),\\
\lambda &= \frac{(\alpha+\beta) + \sqrt{(\alpha-\beta)^2+4\tilde{\delta}^2}}{2} = \frac{(\alpha+\beta) + \sqrt{(\alpha-\beta)^2+4(\alpha-1)(\beta-1)}}{2},\\
\xi &= \text{height of tent} = \frac{1}{4}\sqrt{\lambda^2-1} = \frac{1}{2}\sqrt{(\alpha+\beta)(\alpha+\beta-2)}.
\end{aligned} \tag{5.3}$$

To model the indenting stage, we have to solve an obstacle problem. Our numerical procedure consists of continuation in the height of the indenter; the indenter is incrementally inserted further and further into the film, and the obstacle problem is solved at each step by using a variant of the Polak-Ribière conjugate gradient method [7, 26] to minimize the energy with the previous solution serving as the initial guess. (See Section 6 for a precise description of this step.) We start with the indenter below the film at $\sigma = 0$ and the film in the flat austenitic phase, and we raise the indenter to fully transform the film at $\sigma = 1$ by

$$\zeta(y_1, y_2, \sigma) = \max\left(0, \eta(y_1, y_2) + \xi(\sigma - 1)\right) \qquad \text{for } (y_1, y_2) \in \Omega = (0,1)\times(0,1),$$

for $\xi = 0.225504$ obtained from (5.3) where

$$\eta(y_1, y_2) = 2\min\left(\xi y_1,\ \xi(1-y_1),\ \xi y_2,\ \xi(1-y_2)\right) \qquad \text{for } (y_1, y_2) \in \Omega = (0,1)\times(0,1).$$

The energy with a penalty for the indenter is then

$$\begin{aligned}\mathcal{E}(y,b,\theta,\sigma) = \kappa\left[\int_\Omega |D(\nabla y|b|b)| + \sqrt{2}\int_{\partial\Omega}|b-b_0|\right] + \int_\Omega \phi(\nabla y|b,\theta)\,dx \\ + \nu\int_\Omega [\zeta(y_1(x),y_2(x),\sigma) - y_3(x)]_+^2\;dx.\end{aligned} \tag{5.4}$$

We numerically solve the indenter problem for a given temperature distribution $\theta : \Omega \to \mathbb{R}$ by minimizing the energy (5.4) over continuous, piecewise linear finite element deformations y and piecewise constant b satisfying the boundary condition

$$y(x) = y_0(x) = (x_1, x_2, 0) \qquad \text{for all } x = (x_1,\, x_2) \in \partial\Omega, \tag{5.5}$$

where Ω is the unit square domain whose one side is determined by the vector e given in (5.3) and where $b_0 = (0,0,1)$. Note that the boundary condition (5.5) corresponds to the fact that outside of the domain Ω the film is attached to the substrate and hence remains in the austenitic phase.

6. Finite Element Approximation of the Indenter Experiment

To describe our finite element approximation of (5.4), we let the elements of a triangulation τ of Ω be denoted by K and the inter-element edges by e. To distinguish between the internal edges of τ and the boundary edges of τ, we shall write $e \subset \Omega$ for the internal edges and $e \subset \partial\Omega$ for the boundary edges. Given an internal edge $e \subset \Omega$ and two elements $K_1, K_2 \in \tau$ sharing the edge e, we define the jump across the edge e of a function ψ by

$$[\![\,\psi\,]\!]_e = \psi_{e,K_1} - \psi_{e,K_2}$$

where ψ_{e,K_i} denotes the trace on e of $\psi|_{K_i}$ for $i = 1,2$. Since only the euclidean norm of the jump will enter the discrete energy below, the sign ambiguity in the definition of the jump will not cause an ambiguity in the description of the energy below. For a boundary edge $e \subset \partial\Omega$, we define $\psi|_e$ to be the trace on e. Finally, we denote by $\mathcal{P}_1(\tau)$ the space of continuous, piecewise linear functions on Ω which are linear on each $K \in \tau$, and by $\mathcal{P}_0(\tau)$ the space of piecewise constant functions on Ω which are constant on each $K \in \tau$. Then, for $(y,b) \in \mathcal{P}_1(\tau)\times\mathcal{P}_0(\tau)$ and $\tilde\theta \in \mathcal{P}_0(\tau)$, the energy (5.4) is well-defined, and we have that

$$\begin{aligned}&\kappa\left[\int_\Omega |D(\nabla y|b|b)| + \sqrt{2}\int_{\partial\Omega}|b-b_0|\right] + \int_\Omega \phi(\nabla y|b,\tilde\theta)\,dx \\ &\quad= \kappa\left(\sum_{e\subset\Omega}\Big|[\![\,(\nabla y|b|b)\,]\!]_e\Big|\,|e| + \sqrt{2}\sum_{e\subset\partial\Omega}\Big|b|_e - b_0|_e\Big|\,|e|\right) + \sum_{K\in\tau}\phi\big((\nabla y|b,\tilde\theta)|_K\big)\,|K|,\end{aligned}$$

where $|e|$ denotes the length of the edge e, $|\cdot|$ denotes the euclidean vector norm, $|K|$ is the area of the element K, and

$$\Big|[\![\,(\nabla y|b|b)\,]\!]_e\Big| = \Big(\big|[\![\,\nabla y\,]\!]_e\big|^2 + 2\,\big|[\![\,b\,]\!]_e\big|^2\Big)^{1/2}.$$

Since the above term is not differentiable everywhere, we have regularized it in our numerical simulations.

We approximate the penalty for the indenter by

$$\nu\sum_{P_j}[\zeta(y_1(P_j),y_2(P_j),\sigma) - y_3(P_j)]_+^2\,\frac{h^2}{4},$$

where P_j denote the nodes of the triangulation τ and where h denotes the diameter of the elements in the (uniform) finite element meshes we use in the computations (Figure 3). Notice that if the

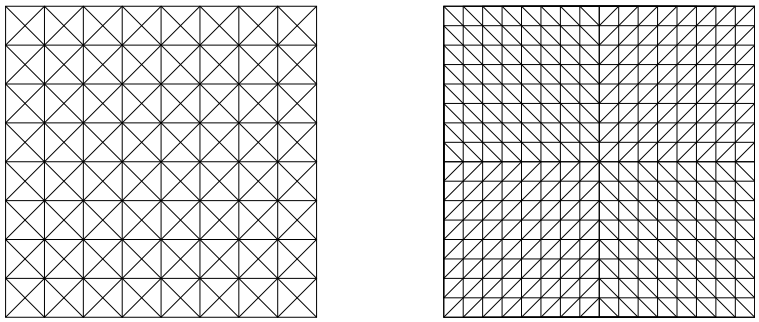

(a) (b)

FIGURE 3. The finite element meshes used in the simulations.

point $(y_1(P_j), y_2(P_j), y_3(P_j))$ lies above the indenter, that is $y_3(P_j) \geq \zeta(y_1(P_j), y_2(P_j), \sigma)$, then the contribution to the penalty function is 0; on the other hand, the contribution is positive for points P_j satisfying $y_3(P_j) < \zeta(y_1(P_j), y_2(P_j), \sigma)$.

To model the action of the indenter, we employ the quasi-static continuation techniques used in our previous computations [7]. As we increment σ from 0 to 1, the indenter is inserted a little deeper into the film, and the augmented energy (5.4) is re-minimized with the previous minimum modified to lie above the indenter serving as the initial guess. More precisely, the initial guess at each node P_j is formed by raising the height $y_3(P_j)$ of the solution at the previous value of σ to $\zeta(y_1(P_j), y_2(P_j), \sigma)$ if it is below this value. We start with the film in the austenitic phase and the indenter removed ($\sigma = 0$). The final stage is with the indenter fully inserted into the film ($\sigma = 1$). At this stage, the film should have been completely transformed to martensite.

7. Numerical Results for the Indenter Experiment

In all of the simulations presented for the indenting and heating process with the energy density ϕ, we have used regular refinements of the finite element mesh shown in Figure 3(a). This mesh is chosen to fully accommodate the fact that the normal to the plane of the reference configuration is a four-fold axis of symmetry of the crystal. Also, the presence of the edges along the diagonals of the square allows for the alignment of the interfaces with that predicted by the theory. Since we seek to study thin films cut or grown along crystallographic planes that allow phase and variant interfaces along specified lines, we have used this information *a priori* in the construction of the finite element mesh.

We note that the mesh in Figure 3(b) biases the alignment of the martensitic interfaces to that expected for the tent, whereas the finite element mesh in Figure 3(a) does not bias the formation of interfaces along either of the diagonals. We have obtained very similar results for the finite element mesh in Figure 3(b) as for the mesh in Figure 3(a) with the energy density ϕ. However, we will see in Figures 7 and 8 that we obtained different results on the two meshes for the simulation of the heating process with the "relaxed" energy density $\bar{\phi}$.

We have displayed results for the criss-cross mesh in Figure 3(a) with $h = 1/48$ and the results for the mesh in Figure 3(b) with $h = \sqrt{2}/64$, where h always denotes the diameter of the largest element of the triangulation. We have utilized the techniques given in [12, 24] to visualize the deformation gradients of the computed deformations.

As the indenting process proceeds, the largest stresses occur at the tip of the indenter; hence, the tip should provide a mechanism for the nucleation of martensite. This is what we also observe in the computed deformations. We fix the temperature of the film at $\theta = -0.3$, that is, slightly below the transformation temperature normalized to $\theta_c = 0$. Due to the stresses caused by the indenter, our computational model is able to simulate the transformation from austenite to martensite.

The simulation was performed with the strain-gradient coefficient $\kappa = 4 \times 10^{-4}$, mesh size $h = 1/48$, and continuation steps in σ equal to $1/94$. Notice that as the indenter penetrates further into the film, more martensite appears and the expected variants (colored red and yellow, respectively, in Figure 4) arrange themselves on the sides of the film and their volume fraction grows (Figure 4(b) and (c)). Finally, when the indenter is fully inserted, the whole film has transformed to martensite, with its sides having deformation gradients in the wells corresponding to U_1 (red) and U_4 (yellow) of (4.3).

When the indenter is removed ($\sigma = 0$) and the energy (5.4) is re-minimized, the film stays in the same tent shape (Figure 4(d)), but the height decreases slightly from $\xi = 0.225504$ to $\xi = 0.225219$. We believe that this small decrease in the height can be explained by the observation that for a small decrease in the height $\xi = 0.225504$ of the tent, the surface energy decreases linearly (up to higher order terms) in the height perturbation since the length of the four tent interfaces is reduced linearly, while the elastic energy increases only quadratically (up to higher order terms) in the height perturbation since the first variation of the elastic energy is zero for the tent with height $\xi = 0.225504$ (note that the deformation gradients are at the bottom of the energy density wells for the tent with height $\xi = 0.225504$).

We have simulated the indenting process without surface energy ($\kappa = 0$) and found results similar to those in Figure 4, but with a slightly more irregular austenite-martensite phase boundary and with other variants occasionally appearing near the interface. We have also simulated the indenting process with the quasi-convex energy density in $\bar{\phi}$ and found results similar to those with ϕ and $\kappa = 0$.

8. Computational Model for the Martensite-to-austenite Phase Transformation by Heating

Since elastic waves propagate and attenuate on a time scale that is fast compared to that of heat conduction [27, 29], we have developed a quasi-static model in which the film is assumed to have reached elastic equilibrium after each time interval during which the temperature has diffused within the film. We assume that the temperature on the boundary is fixed at a constant value, $\theta_{\partial\Omega}$, above the transformation temperature, θ_c. We make the simplifying assumption that the heat diffuses in the reference configuration instead of the deformed configuration, and we model the evolution of the temperature $\theta(x,t)$ by the heat equation

$$\begin{aligned} \theta_t(x,t) &= \mu\,\Delta\theta(x,t) && \text{for } (x,t) \in \Omega \times (0,+\infty), \\ \theta(x,t) &= \theta_{\partial\Omega} && \text{for } (x,t) \in \partial\Omega \times (0,+\infty), \\ \theta(x,0) &= \theta_{\text{init}} && \text{for } x \in \Omega, \end{aligned} \tag{8.1}$$

where $\theta_{\text{init}} < \theta_c$ is the constant initial temperature of the film. Here, μ is the diffusivity coefficient which we can take equal to 1 by scaling time. The greatest simplifying assumption in this treatment of the thermal diffusion is the neglect of the latent heat of the transformation which could be expected to slow the kinetics of the transformation.

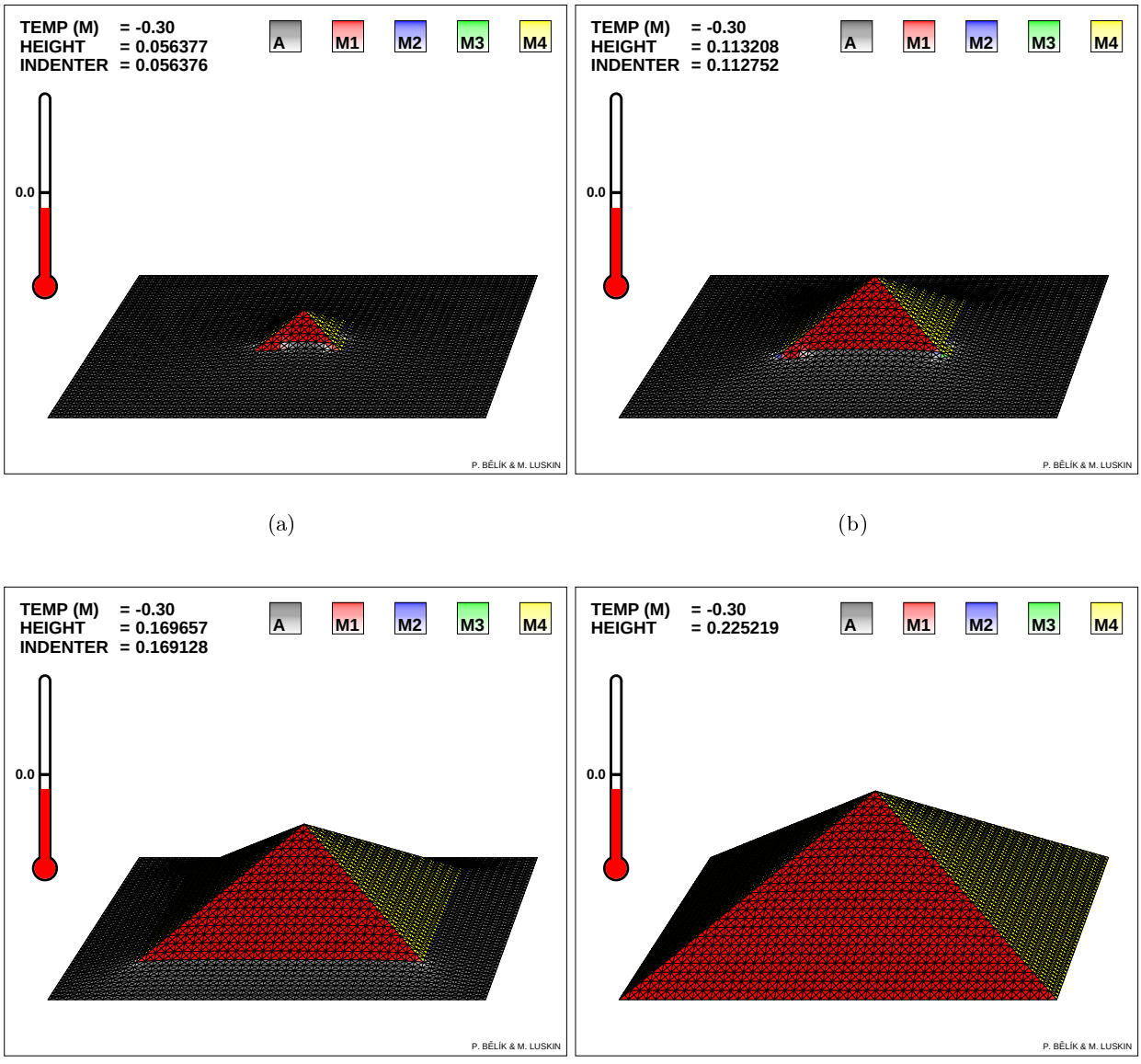

FIGURE 4. The indenting phase of the experiment at $\theta = -0.3$ with $\kappa = 4 \times 10^{-4}$ and $h = 1/48$. The tip of the indenter provides a mechanism for nucleation of the martensite (a) when the indenter is inserted sufficiently far into the film. Upon further penetration of the indenter, more martensite appears and the compatible variants align on the appropriate sides of the tent (b), (c). Notice that the part of the film that is still in austenite is strained, which is exhibited by the lighter shade of gray. When the indenter is fully inserted, the film is completely transformed to martensite. When the indenter is removed and the energy is re-minimized, the shape of the tent remains practically unchanged (d).

Since $\Omega = (0,1) \times (0,1)$, we have for $\theta_{\partial\Omega} = 0$ and $\theta_{\text{init}} = 1$ the analytic solution $\tilde{\theta}(x_1, x_2, t) = \Theta(x_1, t)\Theta(x_2, t)$ for $x = (x_1, x_2) \in \Omega$ given by separation of variables where

$$\Theta(y,t) = \left(\frac{4}{\pi}\right) \sum_{m \text{ odd}} e^{-\mu t \pi^2 m^2} \frac{\sin(m\pi y)}{m}, \qquad y \in (0,1),\ t > 0.$$

Therefore, the solution to (8.1) is given by

$$\theta(x,t) = \tilde{\theta}(x,t)(\theta_{\text{init}} - \theta_{\partial\Omega}) + \theta_{\partial\Omega}.$$

Since the terms in the series decay rapidly for $t > 0$, we use the analytic solution above to evaluate the temperature at each desired time so that the error is on the order of the machine precision.

To model the deformation during the heating of the film, we discretize time during the process by partitioning $[0,T]$ for $T > 0$ by $0 = t_0 < t_1 < \cdots < t_{L-1} < t_L = T$. We then obtain the deformation $(y(t_\ell), b(t_\ell)) \in \mathcal{A}_\tau$ for $\ell = 0, \ldots, L$ by computing a local minimum for the energy $\mathcal{E}(v, c, \theta(t_\ell))$ by the Polak-Ribière conjugate gradient method [26] where $\mathcal{E}(v, c, \theta(t_\ell))$ is the thin film energy

$$\mathcal{E}(v, c, \theta(t_\ell)) = \kappa \left[\int_\Omega |D(\nabla v | c | c)| + \sqrt{2} \int_{\partial\Omega} |c - b_0| \right] + \int_\Omega \phi(\nabla v | c, \theta(t_\ell)) \tag{8.2}$$

defined for the space of approximate admissible deformations

$$\mathcal{A}_\tau = \{(v,c) \in \mathcal{P}_1(\tau) \times \mathcal{P}_0(\tau) :\ v = y_0 \text{ on } \partial\Omega\} \tag{8.3}$$

where

$$\begin{aligned} y_0(x) &= (x_1, x_2, 0) \qquad \text{for } x = (x_1, x_2) \in \partial\Omega, \\ b_0(x) &= (0,0,1) \qquad \text{for } x = (x_1, x_2) \in \partial\Omega. \end{aligned}$$

Since the martensitic transformation strains $\mathcal{U} \subset \mathbb{R}^{3\times 3}$ are local minimizers for the energy density $\phi(F, \theta)$ for all $\theta \in (\theta_0, \theta_1)$, the tent deformation will continue to be a local minimum for the bulk energy $\mathcal{E}(v, c, \theta(t))$ for all $t \geq 0$. Thus, our computational model will not simulate a transforming film if we compute $(y(t_\ell), b(t_\ell)) \in \mathcal{A}_\tau$ by using an energy-decreasing algorithm (such as the Polak-Ribière conjugate gradient method [26]) with the initial state for the iteration at t_ℓ given by the deformation at $t_{\ell-1}$, that is, if $(y^{[0]}(t_\ell), b^{[0]}(t_\ell)) = (y(t_{\ell-1}), b(t_{\ell-1}))$. For this reason, we have developed and utilized an algorithm to nucleate regions of austenite into $(y(t_{\ell-1}), b(t_{\ell-1})) \in \mathcal{A}_\tau$ to obtain an initial iterate $(y^{[0]}(t_\ell), b^{[0]}(t_\ell)) \in \mathcal{A}_\tau$ for the computation of $(y(t_\ell), b(t_\ell)) \in \mathcal{A}_\tau$.

The volume fraction of austenite in a crystal near the transformation temperature θ_C depends on the history of the temperature [29, 30]. The volume fraction of austenite will increase from zero to one if the crystal is initially in a martensitic state at a temperature sufficiently below θ_C and is then heated slowly to a temperature sufficiently above θ_C. To model this behavior, we cycled through the elements of the triangulation τ and used an "equilibrium distribution" function, $P(\theta)$, to determine the probability that the crystal will be in either the austenitic or martensitic phase at a temperature θ in that element with the property

$$P(\theta) \to 0 \text{ as } \theta \to -\infty \quad \text{ and } \quad P(\theta) \to 1 \text{ as } \theta \to \infty.$$

Motivated by equilibrium statistical mechanics [25], we have constructed $P(\theta)$ by the approximation

$$P(\theta) = \frac{e^{\tilde{\beta}(\theta - \theta_c)}}{1 + e^{\tilde{\beta}(\theta - \theta_c)}} \approx \frac{e^{-\tilde{\beta}(\phi(\text{austenite},\theta) - \phi(\text{martensite},\theta))}}{1 + e^{-\tilde{\beta}(\phi(\text{austenite},\theta) - \phi(\text{martensite},\theta))}} = \frac{e^{-\tilde{\beta}\phi(\text{austenite},\theta)}}{e^{-\tilde{\beta}\phi(\text{austenite},\theta)} + e^{-\tilde{\beta}\phi(\text{martensite},\theta)}}$$

where $\phi(\text{austenite}, \theta) = \phi(U_1, \theta) = \cdots = \phi(U_4, \theta)$ and $\phi(\text{martensite}, \theta) = \phi(I, \theta)$. We note that in this model the temperature has been scaled so that

$$\phi(\text{austenite}, \theta) - \phi(\text{martensite}, \theta) \approx (\theta - \theta_C) \qquad \text{for } \theta \text{ near } \theta_C.$$

We describe below how a history dependent distribution function for the volume fraction of austenite can be used in our algorithm.

In our computations, we have set $\tilde{\beta} = 20$ for which the width of the annular region where $0.1 < P(\theta) < 0.9$ is about $2h$ at $t = 1.2 \times 10^{-2}$ and about $5h$ at $t = 4.8 \times 10^{-2}$ in the computations shown in Figures 5–8. We note that a deterministic version of our algorithm can be obtained from the limit $\tilde{\beta} \to \infty$ by setting

$$\begin{cases} P(\theta) = 0 & \text{for } \theta \le \theta_c, \\ P(\theta) = 1 & \text{for } \theta > \theta_c. \end{cases}$$

We use (4.4) to determine the phase of a state $(F, \theta) \in \mathbb{R}^{3\times 3} \times (\theta_0, \theta_1)$. We say (F, θ) is in the austenitic phase if

$$\begin{cases} W_A(F) < W_M(F) + \dfrac{(\theta - \theta_c) W_A(U_1)}{W_A(U_1) + (\theta - \theta_c)} & \text{for } \theta \ge \theta_c, \\ W_A(F) + \dfrac{(\theta_c - \theta) W_M(I)}{W_M(I) + (\theta_c - \theta)} < W_M(F) & \text{for } \theta < \theta_c. \end{cases}$$

Otherwise, we say that (F, θ) is in the martensitic phase.

We observe from (4.3), that if $F \in \mathcal{U}$, then $|Fe_3| = \gamma^2$ and $Fe_1 \cdot Fe_3 = Fe_2 \cdot Fe_3 = 0$. Also, if $F \in \mathrm{SO}(3)$, then $|Fe_3| = 1$ and $Fe_1 \cdot Fe_3 = Fe_2 \cdot Fe_3 = 0$. Hence, if $(\nabla y(x, t_{\ell-1}) | b(x, t_{\ell-1}))$ is near the martensitic well $\mathcal{U}$, then $(\nabla y(x, t_{\ell-1}) | \hat{b})$ will generally be nearer the austenitic well $\mathrm{SO}(3)$ if

$$\hat{b} = \frac{y_{,1}(x, t_{\ell-1}) \times y_{,2}(x, t_{\ell-1})}{|y_{,1}(x, t_{\ell-1}) \times y_{,2}(x, t_{\ell-1})|}.$$

Also, if $(\nabla y(x, t_{\ell-1}) | b(x, t_{\ell-1}))$ is near the austenitic well $\mathrm{SO}(3)$, then $(\nabla y(x, t_{\ell-1}) | \hat{b})$ will generally be nearer the martensitic well $\mathcal{U}$ if

$$\hat{b} = \gamma \, \frac{y_{,1}(x, t_{\ell-1}) \times y_{,2}(x, t_{\ell-1})}{|y_{,1}(x, t_{\ell-1}) \times y_{,2}(x, t_{\ell-1})|}.$$

To compute $(y^{[0]}(t_\ell), b^{[0]}(t_\ell)) \in \mathcal{A}_\tau$, we first compute a pseudo-random number, $\sigma(K, \ell) \in (0, 1)$, on each triangle $K \in \tau$. We then set

$$y^{[0]}(t_\ell) = y(t_{\ell-1}) \in \mathcal{P}_1(\tau)$$

and compute the piecewise constant $b^{[0]}(t_\ell) \in \mathcal{P}_0(\tau)$ by computing $b^{[0]}(x_K, t_\ell) \in \mathbb{R}^3$ on each $K \in \tau$ by (x_K denotes the barycenter of K):

(1) If $\sigma(K, \ell) \le P\left(\theta(x_K, t_\ell)\right)$ and $(\nabla y(x_K, t_{\ell-1}) | b(x_K, t_{\ell-1}), \theta(x_K, t_\ell))$ is in austenite, then set

$$b^{[0]}(x_K, t_\ell) = b(x_K, t_{\ell-1}) \text{ on } K.$$

(2) If $\sigma(K, \ell) \le P\left(\theta(x_K, t_\ell)\right)$ and $(\nabla y(x_K, t_{\ell-1}) | b(x_K, t_{\ell-1}), \theta(x_K, t_\ell))$ is in martensite, then set

$$b^{[0]}(x_K, t_\ell) = \frac{y_{,1}(x_K, t_{\ell-1}) \times y_{,2}(x_K, t_{\ell-1})}{|y_{,1}(x_K, t_{\ell-1}) \times y_{,2}(x_K, t_{\ell-1})|} \qquad \text{on } K.$$

(3) If $\sigma(K, \ell) > P\left(\theta(x_K, t_\ell)\right)$ and $(\nabla y(x_K, t_{\ell-1}) | b(x_K, t_{\ell-1}), \theta(x_K, t_\ell))$ is in austenite, then set

$$b^{[0]}(x_K, t_\ell) = \gamma \, \frac{y_{,1}(x_K, t_{\ell-1}) \times y_{,2}(x_K, t_{\ell-1})}{|y_{,1}(x_K, t_{\ell-1}) \times y_{,2}(x_K, t_{\ell-1})|} \qquad \text{on } K.$$

(4) If $\sigma(K, \ell) > P\left(\theta(x_K, t_\ell)\right)$ and $(\nabla y(x_K, t_{\ell-1}) | b(x_K, t_{\ell-1}), \theta(x_K, t_\ell))$ is in martensite, then set

$$b^{[0]}(x_K, t_\ell) = b(x_K, t_{\ell-1}) \text{ on } K.$$

We then compute the conjugate gradient iterations $(y^{[m]}(t_\ell), b^{[m]}(t_\ell)) \in \mathcal{A}_\tau$ for $m = 1, 2, \ldots$ which converge to the local minimum $(y(t_\ell), b(t_\ell)) \in \mathcal{A}_\tau$ of the thin film energy $\mathcal{E}(v, c, \theta(t_\ell))$ in the energy well (with respect to A_τ) of the initial iterate $(y^{[0]}(t_\ell), b^{[0]}(t_\ell)) \in \mathcal{A}_\tau$. The state of an element $K \in \tau$ will transform back to martensite during the energy-decreasing conjugate gradient interations even though the above "nucleation" step has transformed $(y^{[0]}(t_\ell), b^{[0]}(t_\ell))$ to austenite on $K \in \tau$ if the transformation is energetically unstable.

We have also experimented with several other versions of the above algorithm for the computation of $b^{[0]}(t_\ell)$. For instance, the above algorithm can be modified to utilize different probability functions $P(\theta)$ in elements with increasing and decreasing temperature. One can also prohibit the transformation from austenite to martensite in an element in which the temperature is increasing or prohibit the transformation from martensite to austenite in an element for which the temperature in decreasing.

9. Computational Results for Phase Transformation by Heating

In this section, we present the results of the numerical simulations of the heating phase for $\theta_{\partial\Omega} = 1$ and $\theta_{\text{init}} = -1$ and compare them to the results of the experiment. In Figure 5, we present the results with the energy density ϕ for $\kappa = 4 \times 10^{-4}$, in Figure 6 with the energy density ϕ for $\kappa = 0$, and in Figures 7 and 8 we present the results of the heating phase with the "relaxed" energy density $\bar{\phi}$. The subfigures labeled with the same letters correspond to results with an identical temperature distribution.

We used the energy (3.4) with various nonnegative values of κ. We present the results with $\kappa = 4 \times 10^{-4}$ and $\kappa = 0$. The differences between the case with $\kappa = 4 \times 10^{-4}$ and $\kappa = 0$ were as expected: the resulting deformations for $\kappa = 0$ had a more irregular austenite-martensite phase boundary and variations in the energy-minimizing deformations extended well beyond just a narrow region near the phase boundary. (This phenomenon could have been expected *a priori*, since any "paper-folding" deformation with the deformation gradient satisfying $(\nabla y(x)|b(x)) = R(x)F$ for some $F \in \mathbb{R}^{3\times 3}$ and $R(x) \in \mathrm{SO}(3)$ has elastic energy independent of $R(x)$ [6].) In the computations with $\kappa > 0$, these variations were suppressed to the extent determined by the size of κ. We have empirically found the value $\kappa = 4 \times 10^{-4}$ to be small enough for the elastic energy to be the dominant term of the total free energy and to be large enough to have an impact both on the results of the minimization and on the speed of convergence of our algorithm. (See also Section 11 for further justification of the value $\kappa = 4 \times 10^{-4}$.)

We have also experimented with the "relaxed" model obtained from the energy density $\bar{\phi}$ given in (4.5). We have found that the elimination of energy barriers in the "relaxed" model has a great impact on the solutions obtained for stationary problems by iterative methods, similar to the impact one would expect for time-dependent problems. We see from Figure 7 (computed with the mesh in Figure 3(a) and $h = 1/48$) and Figure 8 (computed with the mesh in Figure 3(b) and $h = \sqrt{2}/64$) that the solution with the "relaxed" energy $\bar{\phi}$ is very sensitive to the mesh orientation. We will propose an explanation for the solution given in Figure 8 in the next section and see that the resulting deformations very closely resemble the deformations in the minimizing sequence constructed in Figure 11.

We observe that the deformation for both meshes immediately becomes round for the simulations with the "relaxed" energy density $\bar{\phi}$, whereas in the experiment the deformation maintained a tent shape until the tent had shrunk to about two-thirds of its original size [14]. On the other hand, the sides of the tent remained sharp during the entire heating process for the energy density ϕ, whereas in the experiment the tent sides seem to become rounded after the tent had shrunk to about two-thirds of its original size. So, although the lack of energy barriers in the energy density

$\bar{\phi}$ seems to make the interfaces too mobile during the early part of the computation, the energy barriers in the energy density ϕ may make the interfaces too immobile in the later stage of the computation.

Comparing Figure 5 with Figure 6, we see that the height of the film was greater when surface energy ($\kappa = 4 \times 10^{-4}$) was included in the model with the energy density ϕ, presumably because it helped to maintain a more rigid tent shape during the heating process. Also, comparing Figures 7 and 8 with Figures 5 and 6, we see that the round shape obtained with the "relaxed" energy density had a height lower than that obtained with the energy density ϕ and no surface energy ($\kappa = 0$).

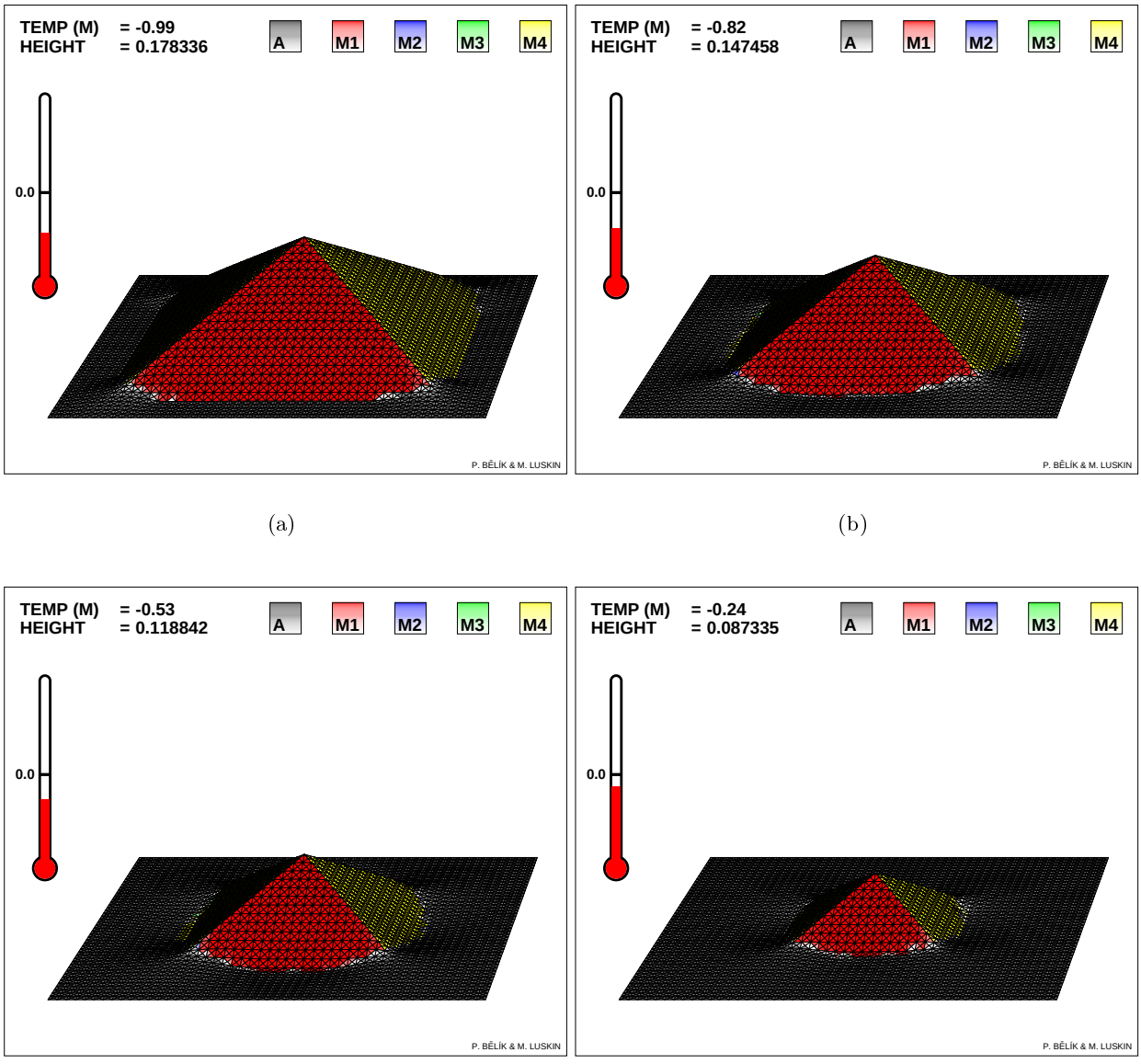

(a) (b)

(c) (d)

FIGURE 5. The heating phase of the experiment at $t = 1.2 \times 10^{-2}$, 2.4×10^{-2}, 3.6×10^{-2}, and 4.8×10^{-2} with $\kappa = 4 \times 10^{-4}$, $h = 1/48$, $\theta_{\partial\Omega} = 1$, $\theta_{\text{init}} = -1$, and $\Delta t = 2.5 \times 10^{-5}$.

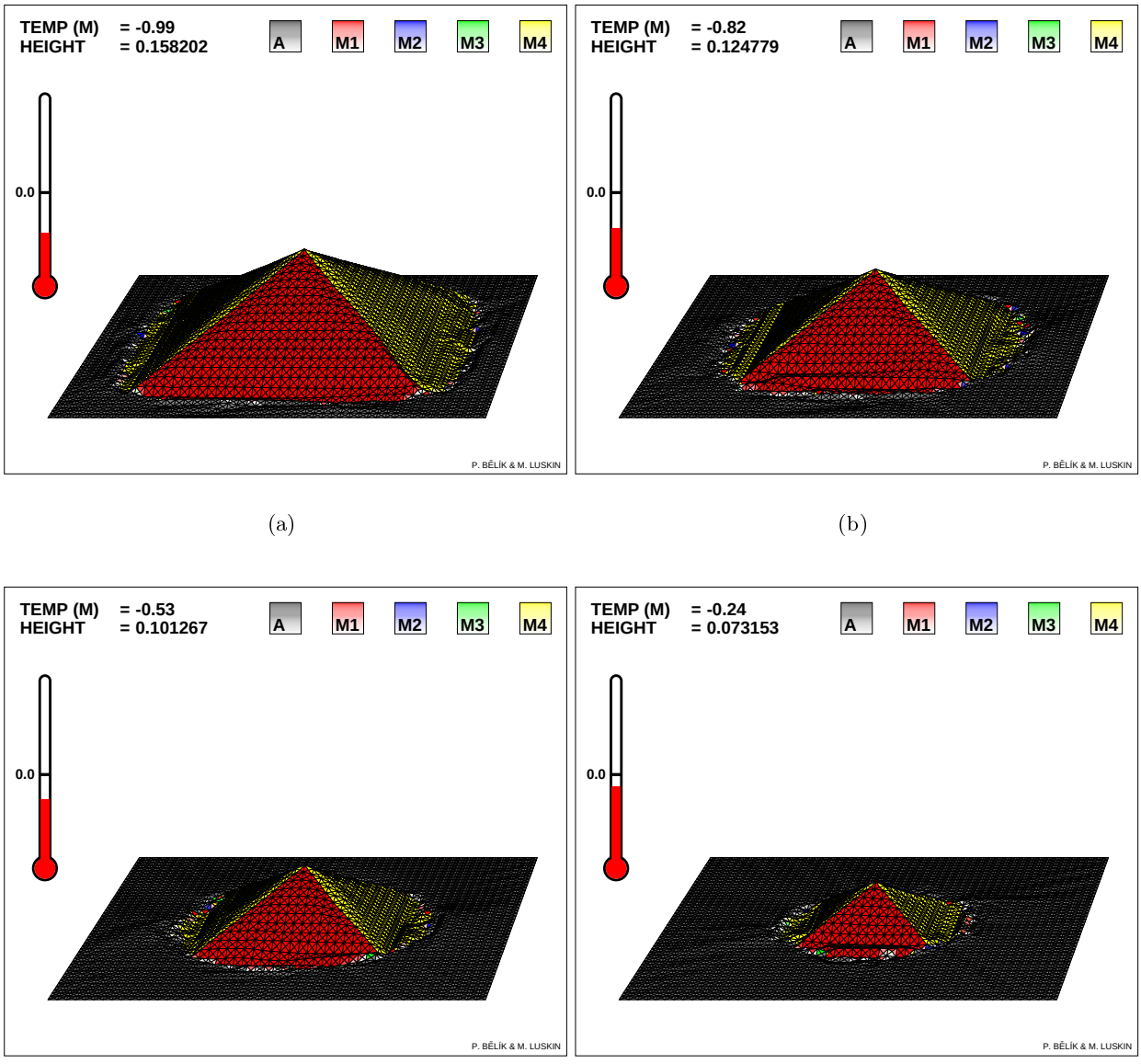

(a) (b)

(c) (d)

FIGURE 6. The heating phase of the experiment at $t = 1.2 \times 10^{-2}$, 2.4×10^{-2}, 3.6×10^{-2}, and 4.8×10^{-2} with $\kappa = 0$, $h = 1/48$, $\theta_{\partial\Omega} = 1$, $\theta_{\text{init}} = -1$, and $\Delta t = 2.5 \times 10^{-5}$.

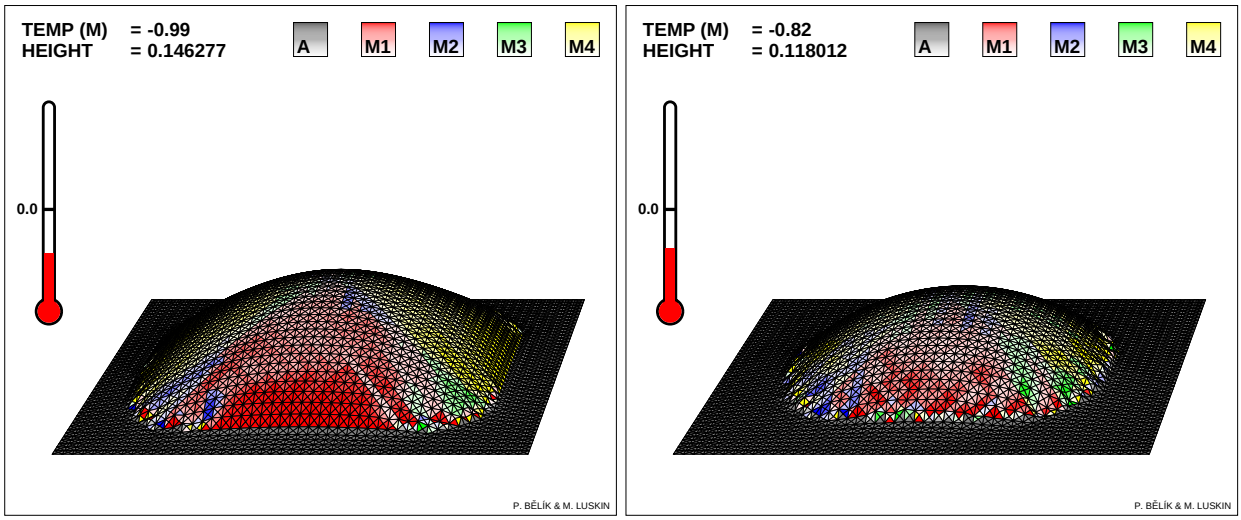

(a) (b)

FIGURE 7. The heating phase of the experiment at $t = 1.2\times10^{-2}$ and 2.4×10^{-2} with the quasi-convex martensitic energy density, $h = 1/48$ for the mesh in Figure 3(a), $\theta_{\partial\Omega} = 1$, $\theta_{\text{init}} = -1$, and $\Delta t = 2.5 \times 10^{-5}$.

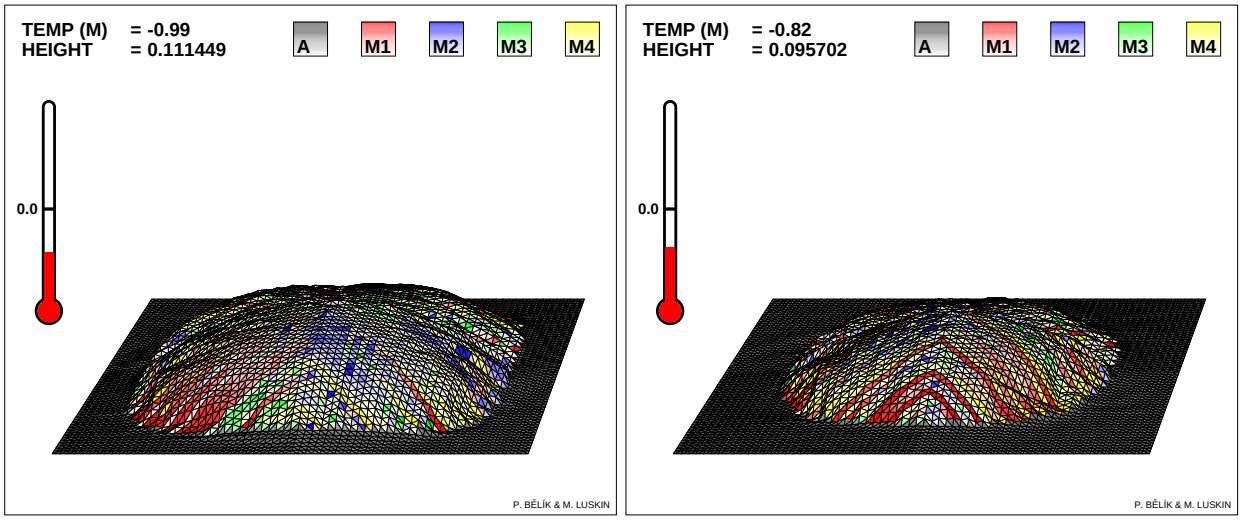

(a) (b)

FIGURE 8. The heating phase of the experiment at $t = 1.2\times10^{-2}$ and 2.4×10^{-2} with the quasi-convex martensitic energy density, $h = \sqrt{2}/64$ for the mesh in Figure 3(b), $\theta_{\partial\Omega} = 1$, $\theta_{\text{init}} = -1$, and $\Delta t = 2.5 \times 10^{-5}$.

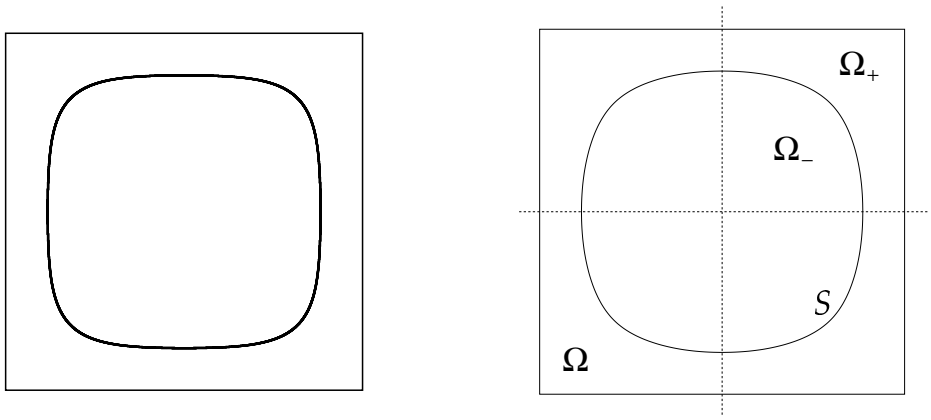

(a) (b)

FIGURE 9. The computed level set $\mathcal{S}(t)$ for the temperature $\theta(x,t) = 0$ at $t = 1.5\times10^{-2}$ and an illustration of the regions $\Omega_-(t)$ where the temperature is negative and $\Omega_+(t)$ where the temperature is positive.

10. Energy-minimizing Sequences for the Heating Process

To discuss the effect of energy barriers, we will assume that $\kappa = 0$ and $\theta_c = 0$. We recall that $\theta(x,t)$ is the solution to (8.1) for constants $\theta_{\partial\Omega} > 0$ and $\theta_{\text{init}} < 0$. We will construct at each $t > 0$ a sequence of admissible deformations $\{(y_k(t), b_k(t))\}$ such that

$$\mathcal{E}(y_k(t), b_k(t), \theta(t)) \to 0 \quad \text{as } k \to \infty. \tag{10.1}$$

Our numerical simulations of the thermally-activated phase transformation of the film modeled with the energy density ϕ have yielded a shrinking tent (Figure 5). On the other hand, our simulations with the "relaxed" energy density $\bar{\phi}$ have given a round deformation (Figure 7) similar to that of our construction (Figure 11). The difference in the computed solutions can be explained by the ability of the iterative method to create and move microstructure as time evolves when there are no energy barriers between the variants.

It is easy to see that at each $t > 0$, the lines $x_1 = 0.5$ and $x_2 = 0.5$ are axes of symmetry of θ, that is,

$$\theta(1-x_1, x_2, t) = \theta(x_1, x_2, t) = \theta(x_1, 1-x_2, t) \quad \text{for all } (x_1, x_2) \in \Omega,\ t > 0. \tag{10.2}$$

Second, Ω is a disjoint union of the sets $\Omega_-(t)$, $\mathcal{S}(t)$, and $\Omega_+(t)$ given by

$$\Omega_-(t) = \{x \in \Omega :\ \theta(x_1, x_2, t) < 0\}, \qquad \Omega_+(t) = \{x \in \Omega :\ \theta(x_1, x_2, t) > 0\},$$
$$\mathcal{S}(t) = \{x \in \Omega :\ \theta(x_1, x_2, t) = 0\},$$

where the level set $\mathcal{S}(t)$ is a convex curve (Figure 9).

To construct the minimizing sequence $\{(y_k(t), b_k(t))\}$ for (10.1), we approximate the level set $\mathcal{S}(t)$ by a polygon whose sides are parallel to the sides of the film, have the symmetry (10.2), and such that the distance between the level set $\mathcal{S}(t)$ and the approximating polygon converges to zero as $k \to \infty$ (Figure 10). We can then construct $\{(y_k(t), b_k(t))\}$ as visualized in Figure 11 such that its deformation gradient takes on the martensitic values $R(\chi, e)U_1$, $R(\chi, n)U_4$, $R(-\chi, e)U_1$, and $R(-\chi, n)U_4$ used to construct the tent in Section 5 inside the approximating polygon and the austenitic deformation gradient I outside the approximating polygon. Clearly, the energy

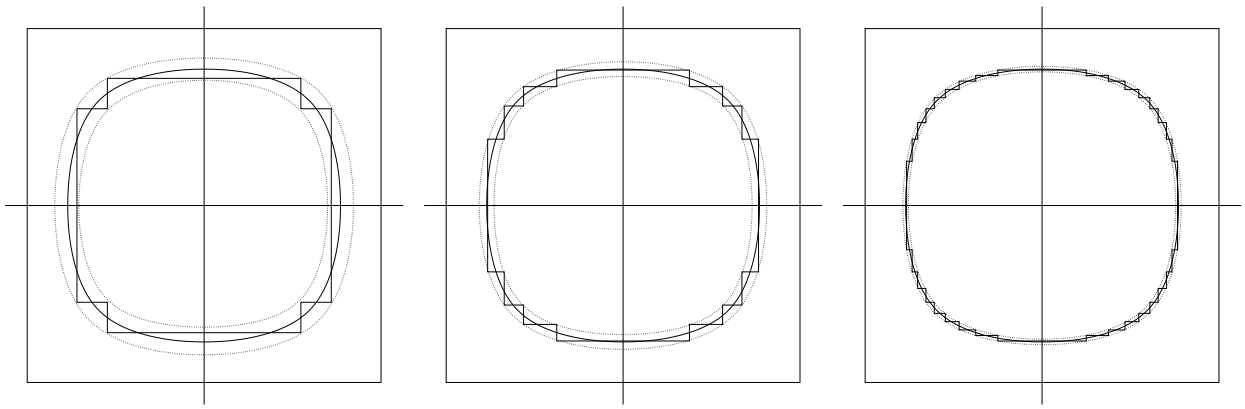

(a) (b) (c)

FIGURE 10. Approximation of $\mathcal{S}(t)$ with a polygon whose sides are parallel to the sides of the square domain.

density of this deformation is minimized outside the thin layer between the curve $\mathcal{S}(t)$ and its approximating polygon; and since the $(\nabla y_k | b_k)$ are uniformly bounded everywhere in Ω, the energy of the deformation in the layer is proportional to the thickness of the layer and hence converges to 0 as $k \to \infty$.

We remark that the volume fractions of the variants (or Young measure [3]) associated with this minimizing sequence can be fully described in terms of the tangents to $\mathcal{S}$ as can be seen from Figure 11. For example, consider the subdomain $(0, 0.5] \times (0, 0.5]$. Denote by $\tau(\tilde{x}) = (\tau_1(\tilde{x}), \tau_2(\tilde{x}))$ the tangent to $\mathcal{S}$ at $\tilde{x}$ scaled so that $|\tau_1| + |\tau_2| = \sqrt{2}$. Denoting the volume fraction of the "red" martensitic variant at a point x by $\lambda_1(x)$ and the volume fraction of the "yellow" martensitic variant by $\lambda_2(x)$, we can easily see that, for $x \in \Omega_- \cap (0, 0.5] \times (0, 0.5]$, in the limit as $k \to \infty$ the volume fractions satisfy $\lambda_1(x) = \tau_1(\tilde{x})$ and $\lambda_2(x) = -\tau_2(\tilde{x})$ where $\tilde{x} \in (0, 0.5] \times (0, 0.5]$ lies on the intersection of $\mathcal{S}$ and the line parallel to $x_2 = x_1$ and passing through x.

We note that the energy-minimizing sequence described above would exhibit immediate rounding off of the edges and the tip of the tent, whereas in the experiment of Cui and James [14] this does not occur until the tent has shrunk to about two-thirds of its size.

11. Computation of Nearly Tent-like Deformations

Finally, we would like to compute the solution to the indenter problem when the orientation of the film or the material constants only approximately satisfy the tent compatibility conditions (5.1). Recall that to satisfy these conditions we use $\tilde{\delta} = \sqrt{(\alpha - 1)(\beta - 1)} \approx 0.0295$, instead of using the measured value $\delta = 0.025$. We will now present results that show what happens if the experimental value $\delta = 0.025$ is retained and used in the computations.

First, it can be checked that there exists no invariant line defined by the $e \in \mathbb{R}^3$ in (5.1) in the reference plane when $\delta = 0.025$. However, as determined in [8], the two wells $\mathrm{SO}(3)U_1$ and $\mathrm{SO}(3)U_4$ are still rank-one connected, that is, $QU_1 - U_4 = a \otimes n$ for some $Q \in \mathrm{SO}(3)$ and $a, n \in \mathbb{R}^3$. Moreover, there exist two distinct solutions Q_1, a_1, n_1 and Q_2, a_2, n_2 with n_1 orthogonal to n_2 and both orthogonal to e_3. The vectors n_1 and n_2 are the normal directions of planar interfaces that separate two regions of constant deformation gradient of a continuous deformation, namely QU_1 and U_4. Hence, it is natural to rotate the square computational domain so that n_1 and n_2 are the

directions of the diagonals of the square. We remark that [8]

$$n_1 = \left(\left(\frac{1}{2} + \frac{\delta}{\sqrt{4\delta^2 + (\alpha-\beta)^2}} \right)^{1/2}, - \left(\frac{1}{2} - \frac{\delta}{\sqrt{4\delta^2 + (\alpha-\beta)^2}} \right)^{1/2}, 0 \right)$$

and that if δ is chosen so that $\delta^2 = (\alpha - 1)(\beta - 1)$, then this orientation coincides with that in Section 5. This orientation will allow for low-energy interfaces between the martensitic variants, but the lack of compatibility between martensite and austenite cannot be overcome by choosing a different computational domain. (The choice of the film orientation in the experiment in [14] was made assuming the alloy satisfies the compatibility conditions exactly, which required a slight theoretical modification of the monoclinic angle.)

In Figure 12, we present the results of simulating the behavior of the film after the indenter has fully deformed the film and then been removed. We present two results, one with no surface energy ($\kappa = 0$) and one with $\kappa = 4 \times 10^{-4}$. The initial guess for these computations is constructed to be exactly the tent-like deformation that should be obtained theoretically if $\delta^2 = (\alpha - 1)(\beta - 1)$.

Figure 12(a) shows the resulting deformation when there is no surface energy. Notice that due to the lack of compatibility between austenite and martensite the sides of the tent are distorted and the height of the tent (0.222131) is slightly below the value expected for a fully compatible tent (0.225504). The drop of the height of the film is a phenomenon also observed in the experiment performed by Cui and James [14] and is probably due to the lack of compatibility—in the experiment and in the model.

Figure 12(b) shows the resulting deformation when $\kappa = 4 \times 10^{-4}$. Notice that the sides of the film are nearly flat. We do not present the results of the similar computations with $\kappa = 10^{-5}$ and $\kappa = 10^{-6}$, but there was no visible flattening effect on the resulting deformation with these choices of κ. Therefore, in all the computations presented above we used κ on the order of 10^{-4}, with the particular choice $\kappa = 4 \times 10^{-4}$ corresponding approximately to h^2 where h is the mesh size.

References

[1] Robert Adams. *Sobolev Spaces*. Academic Press, New York-London, 1975.

[2] John M. Ball and Richard D. James. Fine phase mixtures as minimizers of energy. *Arch. Rational Mech. Anal.*, 100(1):13–52, 1987.

[3] John M. Ball and Richard D. James. Proposed experimental tests of a theory of fine microstructure and the two-well problem. *Phil. Trans. R. Soc. Lond. A*, 338:389–450, 1992.

[4] Kaushik Bhattacharya and Georg Dolzmann. Relaxed constitutive relations for phase transforming materials. *J. Mech. Phys. Solids*, 48(6-7):1493–1517, 2000.

[5] Kaushik Bhattacharya and Georg Dolzmann. Relaxation of some multiwell problems. *Proc. R. Soc. Edinburgh: Section A*, 131:279–320, 2001.

[6] Kaushik Bhattacharya and Richard D. James. A theory of thin films of martensitic materials with applications to microactuators. *J. Mech. Phys. Solids*, 47(3):531–576, 1999.

[7] Pavel Bělík, Tim Brule, and Mitchell Luskin. On the numerical modeling of deformations of pressurized martensitic thin films. *M2AN, Math. Model. Numer. Anal.*, 35(3):525–548, 2001.

[8] Pavel Bělík and Mitchell Luskin. Stability of microstructure for tetragonal to monoclinic martensitic transformations. *M2AN, Math. Model. Numer. Anal.*, 34(3):663–685, 2000.

[9] Pavel Bělík and Mitchell Luskin. A total-variation surface energy model for thin films of martensitic crystals. *Interfaces and Free Boundaries*, to appear.

[10] S. Chakravorty and C. M. Wayman. Electron microscopy of internally faulted Cu-Zn-Al martensite. *Acta. Metall.*, 25:989–1000, 1997.

[11] Charles Collins. Computation of twinning. In David Kinderlehrer, Richard James, Mitchell Luskin, and Jerry L. Ericksen, editors, *Microstructure and Phase Transition*, volume 54 of *The IMA Volumes in Mathematics and its Applications*, pages 39–50. Springer-Verlag, New York, 1993.

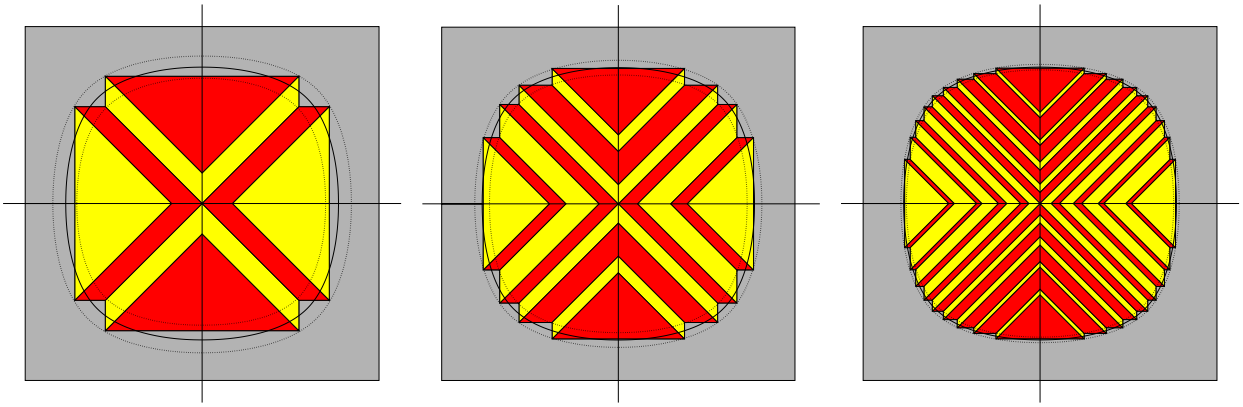

(a) (b) (c)

FIGURE 11. Construction of an energy-minimizing sequence of deformations for a given temperature distribution by combining two compatible variants of martensite inside the curve $\mathcal{S}$ and austenite outside.

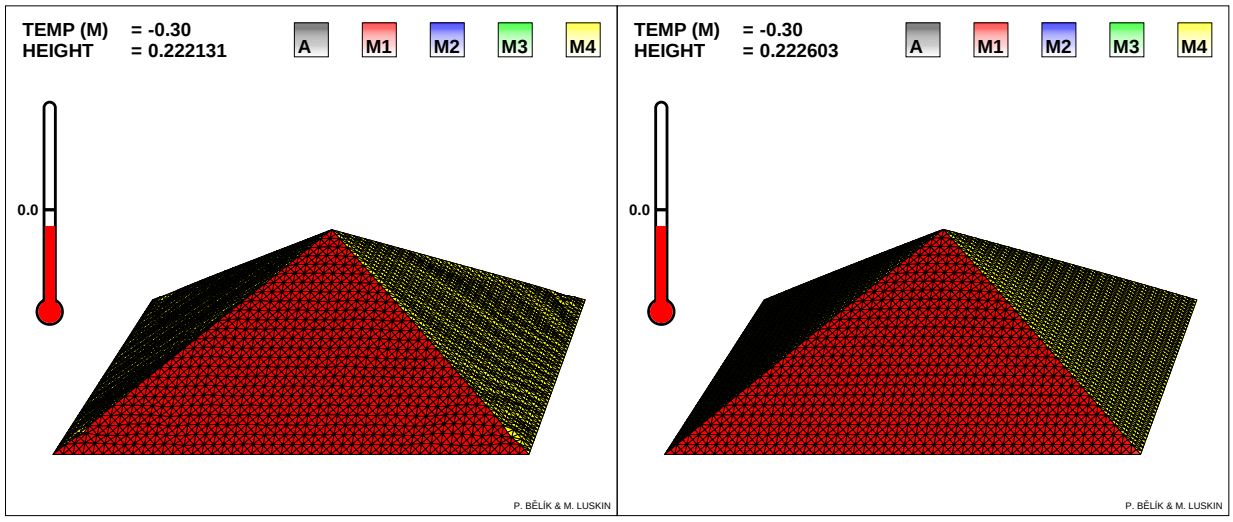

(a) (b)

FIGURE 12. The deformation of the thin film after the indenter has been fully inserted and then removed for the experimental value of $\delta = 0.025$ at temperature $\theta = -0.3$ with mesh size $h = 1/48$. The deformation (a) was obtained with no surface energy ($\kappa = 0$) and the deformation (b) was obtained with $\kappa = 4 \times 10^{-4}$. The sides of the tent are distorted when no surface energy is used, but they are nearly flat for $\kappa = 4 \times 10^{-4}$.

[12] Charles Collins and Mitchell Luskin. The computation of the austenitic-martensitic phase transition. In M. Rascle, D. Serre, and M. Slemrod, editors, *Partial Differential Equations and Continuum Models of Phase Transition*, volume 344 of *Lecture Notes in Physics*, pages 34–50. Springer-Verlag, Berlin-New York, 1989.

[13] Charles Collins, Mitchell Luskin, and James Riordan. Computational results for a two-dimensional model of crystalline microstructure. In David Kinderlehrer, Richard James, Mitchell Luskin, and Jerry L. Ericksen, editors, *Microstructure and Phase Transition*, volume 54 of *The IMA Volumes in Mathematics and its Applications*, pages 51–56. Springer-Verlag, New York, 1993.

[14] Jun Cui and Richard D. James. A "tent" shape thermoelastic deformation on foil of CuAlNi single crystal. Manuscript, 2000.

[15] J. W. Dong, L. C. Chen, C. J. Palmstrøm, R. D. James, and S. McKernan. Molecular beam epitaxy growth of ferromagnetic single crystal (001) Ni_2MnGa on (001) GaAs. *Appl. Phys. Lett.*, 75:1443–45, 1999.

[16] G. Guenin, M. Morin, P. F. Gobin, W. Dejonghe, and L. Delaey. Elastic constant measurements in β Cu-Zn-Al near the martensitic transformation temperature. *Scripta metallurgica*, 11:1071–1075, 1977.

[17] Morton E. Gurtin. *Topics in Finite Elasticity*, volume 35 of *CBMS-NSF Regional Conference Series in Applied Mathematics*. Society for Industrial and Applied Mathematics, Philadelphia, Pa., 1981.

[18] Kevin F. Hane. Bulk and thin film microstructures in untwinned martensites. *J. Mech. Phys. Solids*, 47(9):1917–1939, 1999.

[19] R. D. James and K. F. Hane. Martensitic transformations and shape-memory materials. *Acta mater.*, pages 197–222, 2000.

[20] Robert Kohn and Stefan Müller. Branching of twins near an austenite–twinned-martensite interface. *Philosophical Magazine A*, 66(5):697–715, 1992.

[21] P. Krulevitch, A. P. Lee, P. B. Ramsey, J. C. Trevino, J. Hamilton, and M. A. Northrup. Thin film shape memory microactuators. *J. MEMS*, 5:270–282, 1996.

[22] Bo Li and Mitchell Luskin. Theory and computation for the microstructure near the interface between twinned layers and a pure variant of martensite. *Materials Science & Engineering A*, 273:237–240, 1999.

[23] A. E. H. Love. *A treatise on the Mathematical Theory of Elasticity*. Dover Publications, New York, fourth edition, 1944.

[24] Mitchell Luskin. On the computation of crystalline microstructure. *Acta Numer.*, 5:191–257, 1996.

[25] Donald A. McQuarrie. *Statistical Mechanics*. Harper & Row, New York, 1976.

[26] Jorge Nocedal and Stephen Wright. *Numerical Optimization*. Springer-Verlag, New York, 1999.

[27] K. Otsuka and C. M. Wayman, editors. *Shape Memory Materials*. Cambridge University Press, 1998.

[28] P. L. Rodriguez, F. C. Lovey, G. Guenin, J. L. Pelegrina, M. Sade, and M. Morin. Elastic constants of the monoclinic 18R martensite of a Cu-Zn-Al alloy. *Acta metall. mater.*, 41(11):3307–3310, 1993.

[29] Kenichi Shimizu and Tsugio Tadaki. *Shape Memory Effect: Mechanism*, volume 1 of *Precision machinery and robotics*, pages 1–60. Gordon and Breach, 1987.

[30] C. M. Wayman. *Introduction to the Crystallography of Martensitic Transformations*. MacMillan, New York, 1964.

Pavel Bělík, School of Mathematics, University of Minnesota, 206 Church Street SE, Minneapolis, MN 55455, U.S.A.

E-mail address: belik@math.umn.edu

Mitchell Luskin, School of Mathematics, University of Minnesota, 206 Church Street SE, Minneapolis, MN 55455, U.S.A.

E-mail address: luskin@math.umn.edu